

## Article

# Effects of Cu-Ni-Ti Interlayer on Microstructure and Wear Resistance around Gas Tungsten Arc Cladding Copper Matrix Composite Coatings on Steel

Jihong Li \*, Longyu Lei, Mingke Du, Zhiqiang Zhang and Min Zhang 

School of Materials Science and Engineering, Xi'an University of Technology, Xi'an 710048, China

\* Correspondence: lijihong@xaut.edu.cn

**Abstract:** Due to the huge difference in thermophysical properties, it is difficult to obtain a defect-free bonding interface between copper and steel. A Cu-Ni-Ti interlayer was added between a TiC-reinforced copper matrix composite coating and Q235 steel in this study to improve its interfacial bond. The influence of the interlayer on its microstructure and properties was studied by characterizing microstructure, phase composition, and wear resistance of the composite coatings. Both coatings were found to consist of  $\alpha$ -Cu matrix, in situ-generated TiC, and Fe-rich phases. With the addition of the Cu-Ni-Ti interlayer, the high-hardness unmixed zone at the interface was successfully eliminated due to the sufficient mixing of the molten pool. Even more importantly, liquid metal embrittlement cracks were also restrained, resulting from the Fe-rich solid solution band that reduced the contact probability around liquid copper atoms with the steel grain boundaries formed. In addition, the results showed that the microhardness of composite coatings was improved and the wear loss reduced by 4.2% after adding that interlayer, which was related to the combined action of solid solution strengthening, second-phase strengthening and grain-refinement strengthening mechanisms.



**Citation:** Li, J.; Lei, L.; Du, M.; Zhang, Z.; Zhang, M. Effects of Cu-Ni-Ti Interlayer on Microstructure and Wear Resistance around Gas Tungsten Arc Cladding Copper Matrix Composite Coatings on Steel. *Coatings* **2022**, *12*, 1360. <https://doi.org/10.3390/coatings12091360>

Academic Editor: Gianni Barucca

Received: 29 August 2022

Accepted: 14 September 2022

Published: 18 September 2022

**Publisher's Note:** MDPI stays neutral with regard to jurisdictional claims in published maps and institutional affiliations.



**Copyright:** © 2022 by the authors. Licensee MDPI, Basel, Switzerland. This article is an open access article distributed under the terms and conditions of the Creative Commons Attribution (CC BY) license (<https://creativecommons.org/licenses/by/4.0/>).

**Keywords:** arc cladding; interlayer; copper–steel interface; unmixed zone; liquid metal embrittlement; wear resistance

## 1. Introduction

With the development of industry, a single material often cannot meet the application requirements due to its performance limitations. Bimetal composites have received more and more attention because they not only have the performance advantages of both materials but also can significantly reduce cost [1,2]. As a typical bimetallic material, the copper–steel composite has thermal conductivity, wear reduction, the corrosion resistance of copper, and the high strength of steel. Because of its superior properties, the copper–steel composite is widely used for aerospace, metallurgy, electric power, and other applications [3,4]. At present, the preparation methods of copper–steel composite structures mainly include explosive bonding [5], diffusion bonding [6], high-energy beam cladding [7], and arc cladding [8,9], etc. Arc cladding is developed based on arc welding and has significant advantages in production efficiency, process adaptability, and cost. However, it is difficult to obtain high-quality copper–steel joints due to the extremely low solubility of copper and iron at room temperature and the great differences in physical properties, such as melting point, thermal conductivity, and coefficient of thermal expansion [10,11].

Although harmful brittle intermetallic compounds will not form in copper–steel joints, there are other problems that affect the properties, such as unmixed zone (UZ) and liquid metal embrittlement (LME) cracks. UZ is common in dissimilar-metal fusion joints, and can be found in dissimilar steels [12], Inconel–steel [13], aluminum alloy–steel [14], Co-based alloy–steel [15], high-entropy alloy–steel [16], and copper–steel [17–19] joints. The formation of UZ is related to the flow state of the liquid metal in the molten pool [20]. For the preparation of copper–steel composites, when the first layer of copper is deposited,

the surface metal of the steel melts under the action of the arc heat source. Due to the viscosity of liquid metals, the liquid iron at the boundary of the molten pool has a low flow velocity, so it cannot be well mixed with the liquid copper. Only a small amount of copper diffuses into the UZ, driven by the concentration gradient, and precipitates during solidification to form copper islands [21]. Finally, a UZ of similar composition to that of the steel substrate is formed. The UZ can reduce the corrosion resistance of joints and lead to uneven mechanical properties [12,22–24]. LME cracks also occur at the copper–steel interface, and have a greater impact on the mechanical properties of copper–steel joints than UZ. LME cracks will cause brittle fracture of the composite structure in an instant, which leads to serious consequences. LME can be described as the reduction in ductility of the solid metal when the solid metal is in contact with another liquid metal with a low melting point [25]. The formation of LME cracks is related to the wetting of the steel grain boundaries by liquid copper and the thermal stress during the cladding process in the Cu-Fe system [26]. LME cracks can propagate along grain boundaries and adversely affect the ductility and fatigue strength of composites [27]. For example, they can lead to brittle fracture of the interface or the steel substrate during operation or premature peeling of the coatings. This will reduce the service life of copper–steel composites. Therefore, in order to obtain high-quality copper–steel joints, measures should be taken to suppress UZ and LME cracks at the interface.

Adding an interlayer between the bimetallic interfaces has played an important role in reducing the interface defects, improving the properties and service life of the composites [28–30]. For copper–steel composite structures, Ni-based or Cu-Ni-based materials can be used as an interlayer to achieve a good connection between them, because Ni has high solid solubility in both Cu and Fe and its thermophysical properties are between them [31,32]. In the current research on copper–steel composites, most of the copper side materials are pure metals or commercial copper alloys. There is little research on the preparation of copper-based composite coatings on steel. Elemental diffusion between the interlayer and the composite coating will change the composition and microstructure of the coating, thus affecting tribological behavior of the coating. However, relevant research is scarce at present. To address the above issues and explore the effect of interlayers on composite coatings, TiC-reinforced copper matrix composite coatings were successfully prepared on Q235 low-carbon steel by gas tungsten arc (GTA) cladding in this study. The effects of the Cu-Ni-Ti interlayer on the microstructure and tribological properties of the composite coatings was studied, which can provide references for the research and engineering applications of copper matrix wear-resistant coatings.

## 2. Materials and Methods

### 2.1. Coating Preparation

Q235 steel with dimensions of 100 mm × 70 mm × 10 mm was used as the substrate, and its chemical composition is listed in Table 1. The cladding materials included Cu-Al-Ti-Sn flux-cored wires for preparing copper matrix composite coatings, Cu-Ni-Ti flux-cored wires for preparing the interlayer, and S214 commercial aluminum–bronze wires for comparison with composite coatings in wear resistance. Al and Sn in the welding wires can strengthen the copper matrix, and Ti can react with C in situ to form TiC, which improves the wear resistance of the coatings [33–35]. All wires were 1.6 mm in diameter, and the chemical compositions are given in Table 2. All coatings were prepared by GTA cladding, as shown in Figure 1a. The cladding current was 150 A. Argon gas (99.99% purity) was used as the shielding gas, and the gas flow rate was 15 L/min.

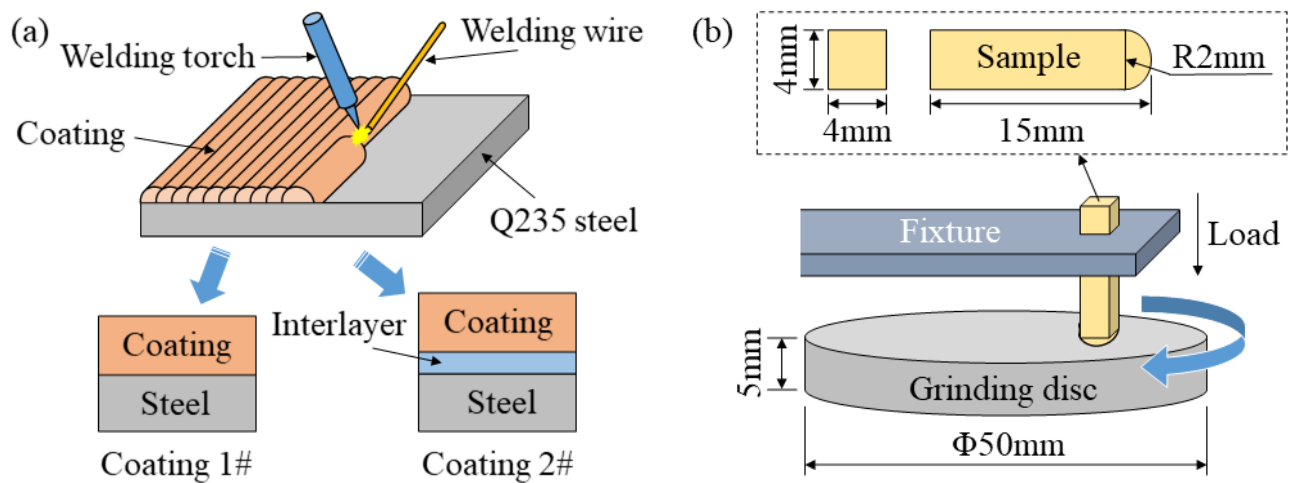


**Figure 1.** Schematic diagram of (a) GTA cladding and (b) wear test and its samples.

**Table 1.** Chemical composition of Q235 steel (wt.%).

C	Mn	Si	S	P	Fe
≤0.22	≤1.40	≤0.35	≤0.05	≤0.045	Bal.

**Table 2.** Chemical composition of the welding wires (wt.%).

Materials	C	Al	Ti	Sn	Ni	Si	Mn	Cu
Coating	0.40	1.00	8.80	4.40	-	0.25	0.25	Bal.
Interlayer	-	-	2.90	/	10.30	0.30	0.30	Bal.
S214	-	7.00–8.50	-	-	-	-	-	Bal.

## 2.2. Microstructure and Property Characterization

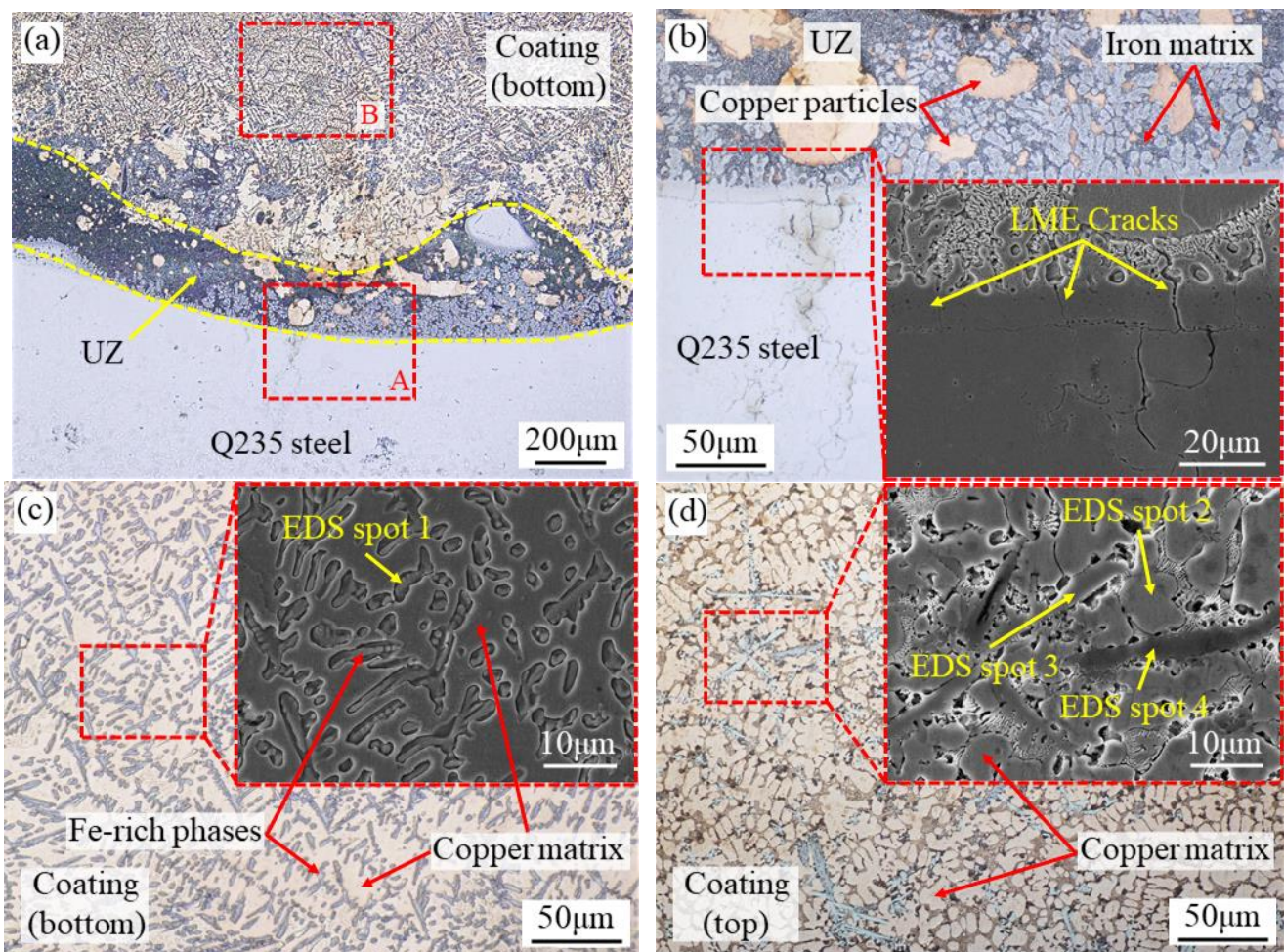
After GTA cladding, test and analysis samples were prepared by a wire-cutting machine. The samples for microstructure and composition analysis of the coatings were etched by 5 g  $\text{FeCl}_3$  + 10 mL HCl + 100 mL  $\text{H}_2\text{O}$  corrosive liquid. Then, an Olympus GX71 optical microscope (OM) and Tescan VEGA3 XMU scanning electron microscope (SEM) equipped with energy-dispersive spectrometer (EDS) were used to characterize the microstructure, composition, and element diffusion mode of the coatings. The phases of the coating surfaces were analyzed by XRD-7000 X-ray diffractometry (XRD) with scanning speed of  $8^\circ/\text{min}$ , step size of  $0.02^\circ$ , and scanning angle of  $20\text{--}90^\circ$ .

The microhardness of the copper matrix composite coatings was tested by an MHV-1000Z Vickers microhardness tester. The load of the microhardness test was 0.1 kgf, and the load-dwell time was 15 s. The wear resistance of the coatings was tested using an HT-1000 friction and wear testing machine with a rotational speed of 350 r/min, a load of 5 N, a friction radius of 5 mm, and a test time of 30 min. The test was conducted in dry and sliding friction conditions at room temperature. The samples were first cut from the coatings and then machined as pins using a lathe. Number 45 steel with a hardness of HRC 42–46 was used as the grinding disk. The schematic diagram of wear test and sample size are shown in Figure 1b. Before and after the test, an electronic analytical balance with an accuracy of 0.1 mg was used to weigh the samples and the wear loss calculated. Then, the morphology of the worn surfaces was characterized by scanning electron microscope to analyze the wear mechanism.

### 3. Results

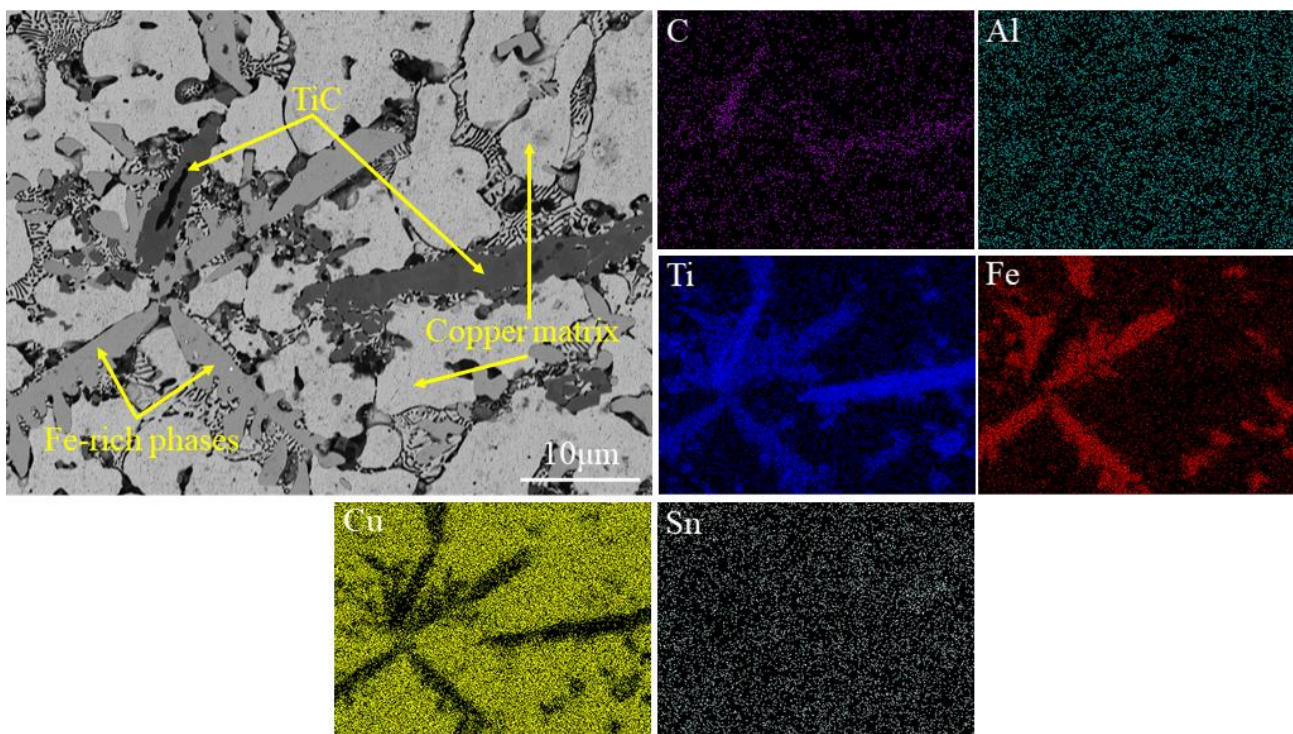
#### 3.1. Microstructure and Phase Constituents

Figure 2 shows the microstructure of coating 1. EDS spot analysis results of spots 1–4 in Figure 2 are shown in Table 3. Figure 2a shows the microstructure of the copper–steel interface. A UZ with a width of about 100–400  $\mu\text{m}$  between the coating and the substrate can be seen, where copper particles of different shapes were found. Figure 2b shows an enlarged view of the UZ–substrate interface in region A of Figure 2a. LME cracks were found at the interface, which adversely affected the bonding strength of the interface. Figure 2c shows a local magnification of region B at the bottom of coating 1 in Figure 2a. It can be seen that a large number of dendritic and equiaxed Fe-rich phases were distributed on the copper matrix (spot 1 in Table 3). The Fe-rich phases formed by the solidification of Fe diffused from the steel into the molten pool. Figure 2d shows the microstructure at the top of coating 1, which is mainly composed of dendrites and a few cellular crystals. The EDS analysis result of spot 2 shows that it is a copper-based solid solution. In addition, there are two kinds of gray phases distributed in the intergranular space. One of them is dendritic with equiaxed light-gray Fe-rich phases (spot 3 in Table 3). The other shows some dark-gray rod-like phases. EDS analysis of spot 4 shows that the dark-gray phases are TiC generated by the in situ reaction of Ti and C, which can enhance the coatings. In general, coating 1 was defect-free, except for LME cracks at the copper–steel interface.



**Figure 2.** Microstructure of coating 1: (a) copper–steel bonding interface, (b) region A in Figure 2a, (c) region B in Figure 2a (bottom of coating 1), (d) top of coating 1.

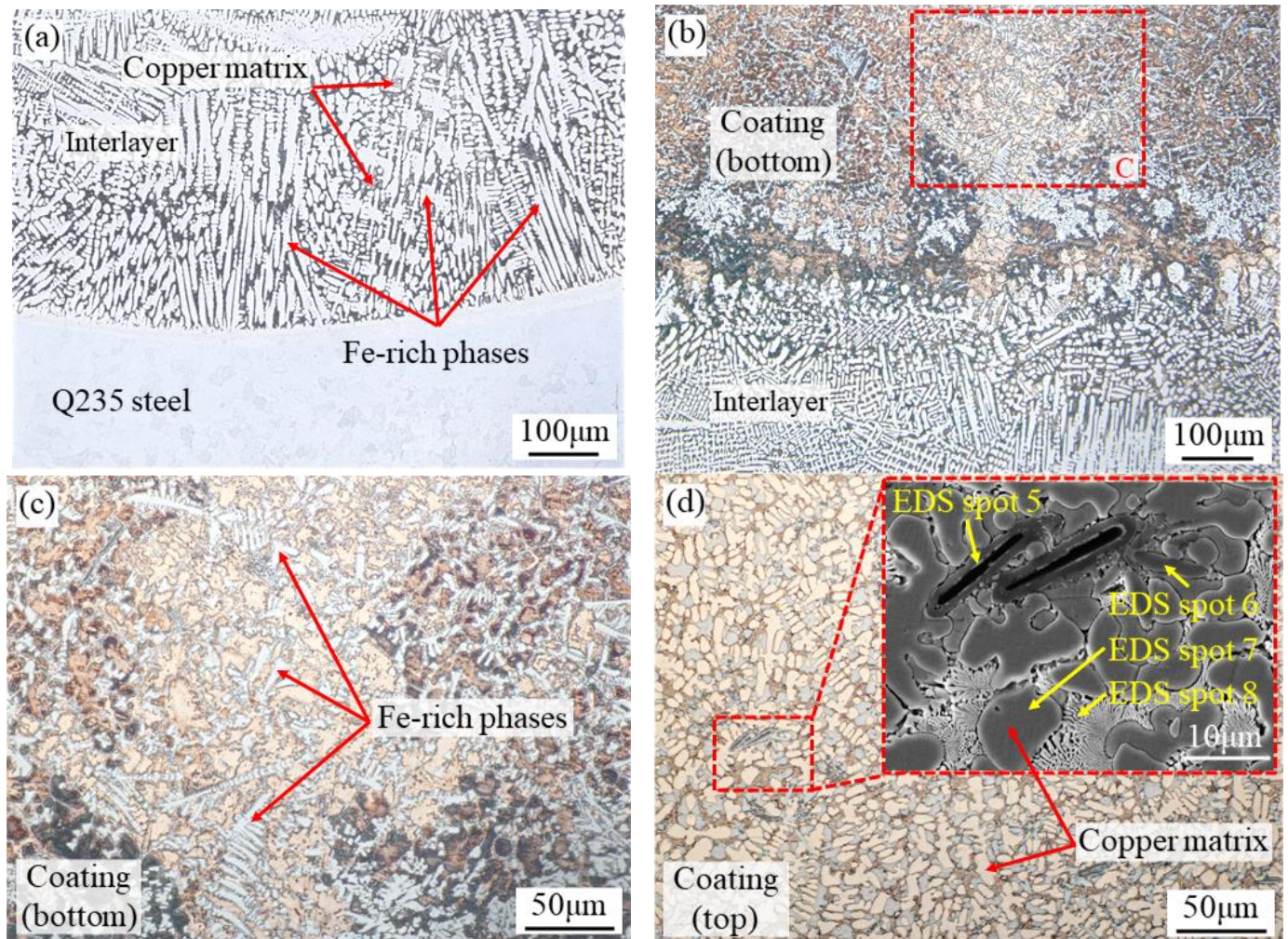
In order to more intuitively characterize the composition distribution at the top of coating 1, the BSE mode of the scanning electron microscope was used to observe the framed selection region in Figure 2d, and the element distribution in this region was analyzed, as shown in Figure 3. The element maps show that the distribution of Ti overlapped with C and Fe, respectively. This indicates that a part of Ti was enriched in the Fe-rich phases, and the other part of Ti reacted with C to generate TiC. The top of coating 1 mainly consists of copper matrix, Fe-rich phases, and TiC reinforcements. As the atomic number of elements in the BSE image is larger, the corresponding color is lighter. Therefore, the large white area in the BSE image is copper matrix, the light-gray dendritic and equiaxed areas are Fe-rich phases, and the dark-gray rod-like phases are TiC, which is the same as the EDS spot analysis results.



**Figure 3.** BSE image and elemental maps of the frame selection region in Figure 2d.

Figure 4 shows the microstructure of coating 2. The microstructure of the interlayer-steel interface is shown in Figure 4a. It can be seen that the interface is well bonded, and no cracks or UZ were found. The microstructure of the interlayer is mainly columnar dendrites growing perpendicularly to the fusion line, which is related to constitutional supercooling and heat-dissipation direction during the solidification of the molten pool. Figure 4b shows the microstructure of the interface between the interlayer and the composite coating. The interlayer and the coating almost reached a gradient transition and a combination of better quality. Figure 4c is an enlarged view of region C at the bottom of coating 2 in Figure 4b. A large number of gray Fe-rich phases are distributed on the copper matrix, and the morphology is mainly dendritic crystals. Figure 4d shows the microstructure at the top of coating 2. The top morphology of coating 2 is basically the same as that of coating 1, but the dendrite and equiaxed crystals are smaller. In addition, the size and number of the light-gray Fe-rich phases in coating 2 are higher than those in coating 1, which is consistent with the results of reference [24]. Based on the results of EDS spot analysis (spots 5–8 in Table 3), BSE image, and element maps of the selected region in Figure 4d (see Figure 5), it can be seen that the distribution of elements C, Ti and Fe on the top of coating 2 is similar to that of coating 1. That is, Ti is enriched in the Fe-rich phases and TiC, respectively. Coating 2 still consists of copper matrix, Fe-rich phases, and TiC reinforcements. There is a relatively uniform distribution of Ni in coating 2, which is different from coating 1. This is because

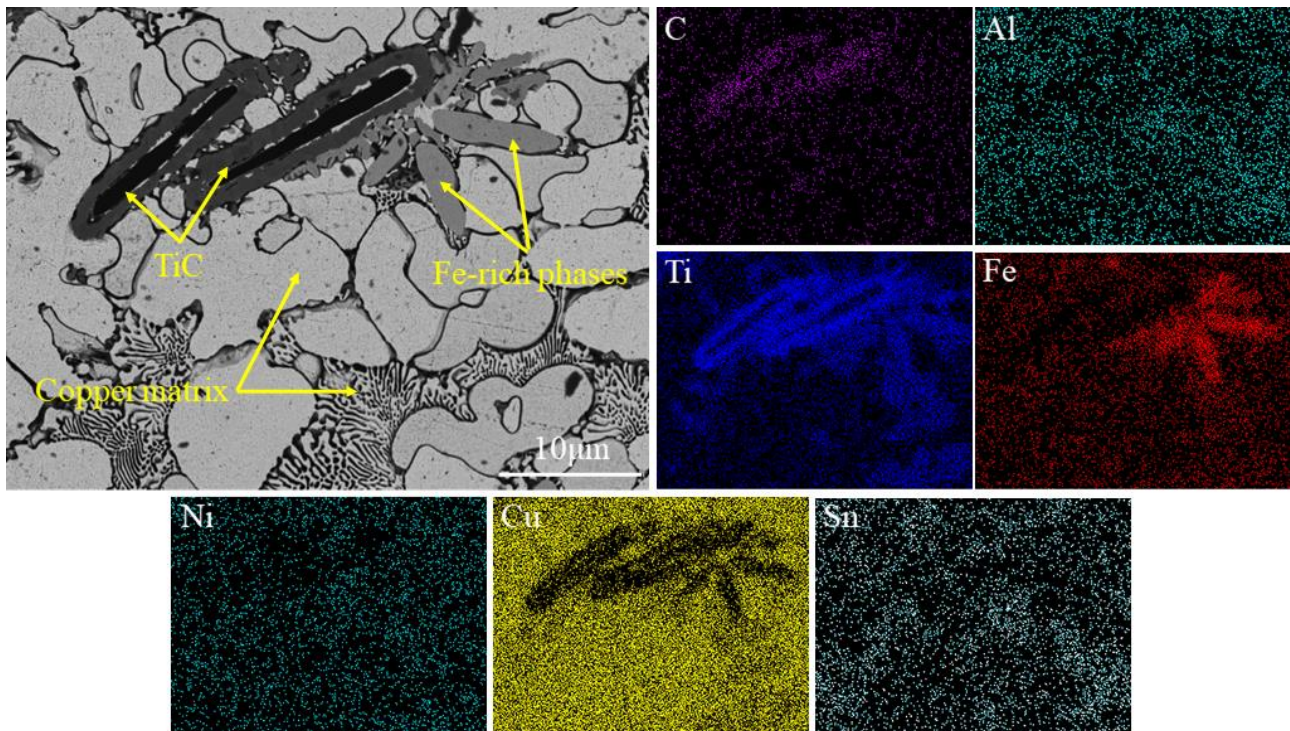
part of Ni in the interlayer entered the composite coating under the action of diffusion and molten pool convection during the cladding process, and was dissolved in the copper matrix. This enables solid solution strengthening of the coating. In summary, the Cu-Ni-Ti interlayer not only eliminated UZ and LME cracks at the interface, but also changed the composition of the coating.



**Figure 4.** Microstructure of coating 2: (a) the connection interface between the steel and interlayer, (b) the connection interface between the interlayer and copper, (c) region C in Figure 4b (bottom of coating 2), (d) top of coating 2.

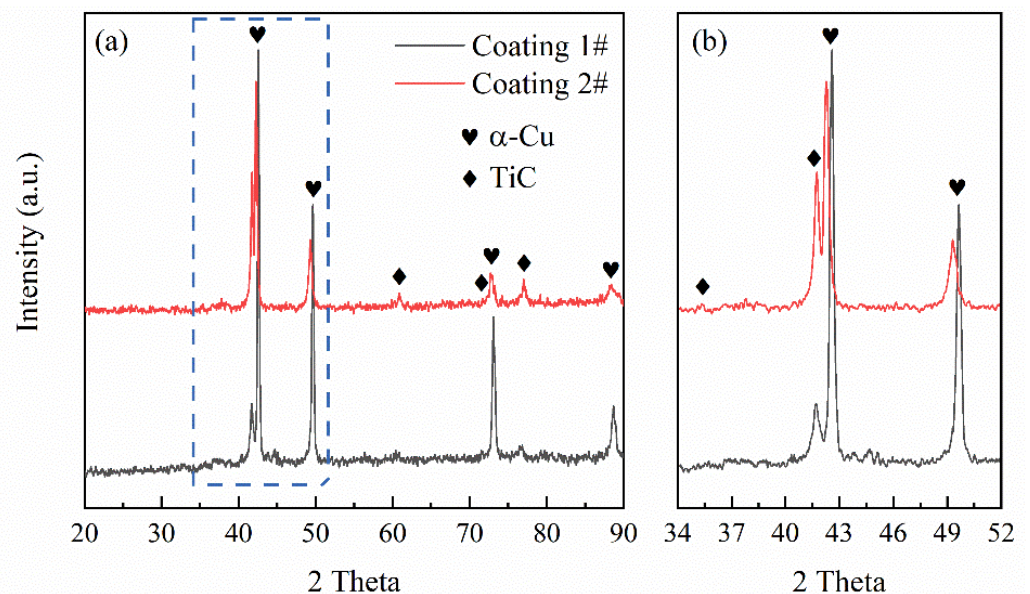
**Table 3.** EDS analysis results of the spots in Figures 2 and 4 (wt.%).

EDS Spots	C K	Al K	Ti K	Fe K	Ni K	Cu K	Sn K
1	-	1.5	29.6	63.4	-	5.1	0.3
2	-	3.1	4.5	1.4	-	90.0	1.0
3	-	2.1	34.6	52.7	-	10.2	0.4
4	10.7	0.3	85.2	0.7	-	3.0	0.1
5	15.5	0.1	77.5	1.8	0.6	4.3	0.2
6	-	2.9	40.5	43.7	3.3	9.2	0.3
7	-	6.4	3.3	1.1	0.6	88.0	0.6
8	-	2.0	3.8	1.0	0.7	92.1	0.4



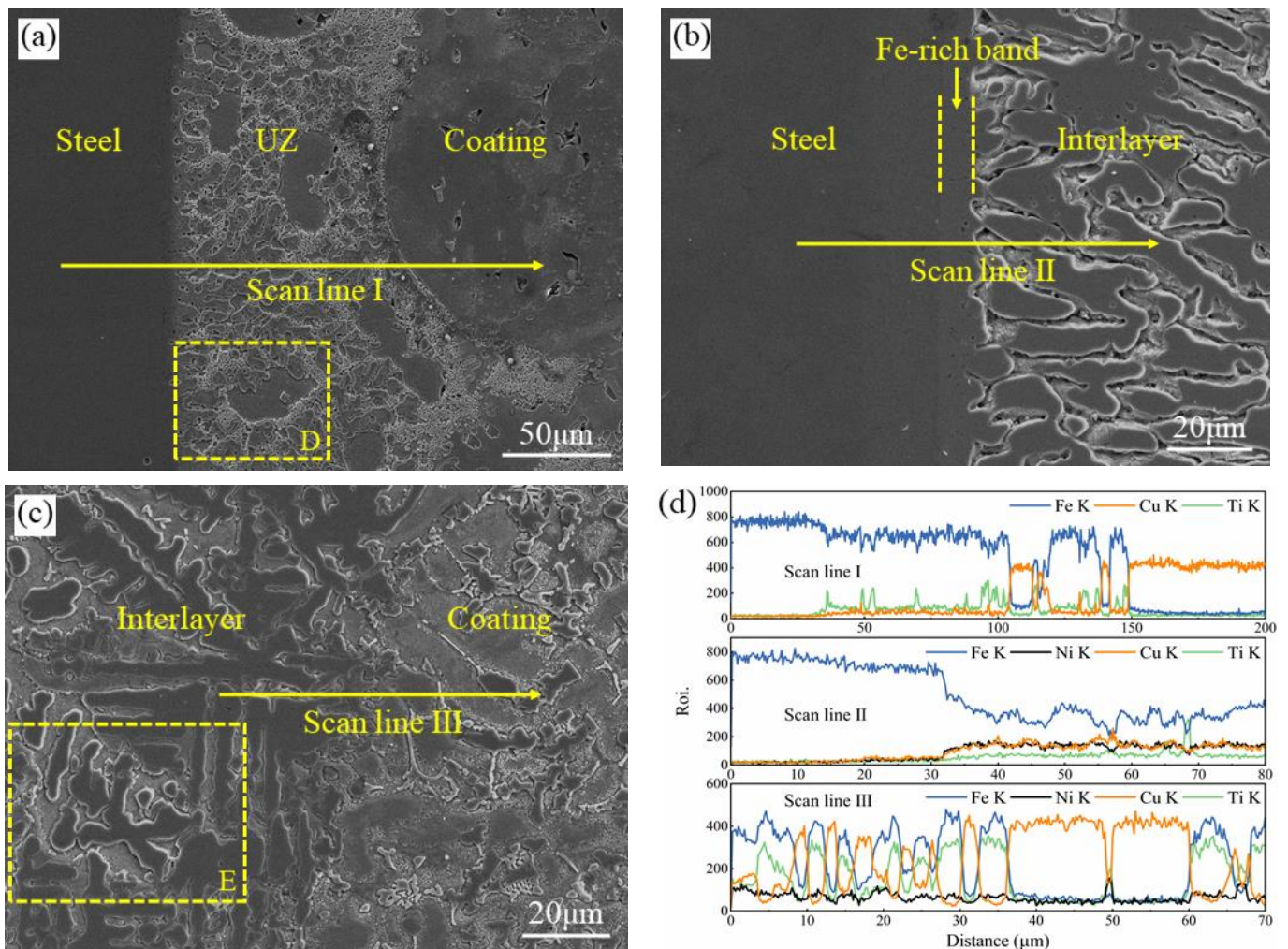
**Figure 5.** BSE image and elemental maps of the frame selection region in Figure 4d.

Figure 6 shows the XRD patterns of coatings 1 and 2. Figure 6a shows the complete XRD patterns, and Figure 6b shows the enlarged view of the selected region in Figure 6a. According to the patterns in Figure 6a, the composite coatings are mainly composed of  $\alpha$ -Cu solid solution and TiC. TiC was formed by the in situ reaction of Ti and C in the molten pool. No diffraction peaks of the Fe-rich phase were found in the figure, which may be related to its low content in two coatings. With the addition of the interlayer, the diffraction peaks of  $\alpha$ -Cu shifted to a smaller angle (Figure 6b). This is because part of Ni from the Cu-Ni-Ti interlayer was dissolved in the  $\alpha$ -Cu matrix of coating 2, which increases the lattice constant of copper.



**Figure 6.** (a) XRD patterns of the tops of coatings 1 and 2, (b) patterns at 34–52° at a larger magnification.

In order to characterize the effect of interlayer on the bonding behavior of the copper–steel interface, elemental diffusion at different interfaces was tested and analyzed by EDS. The corresponding SEM images and EDS line-scan results are shown in Figure 7. Figure 7a is the SEM image of the interface in coating 1, and Figure 7b,c are the SEM images of the interfaces in coating 2. Combining Figure 7a,b, it can be seen that the interface between copper and steel from the initial single transition form a continuous transition after the addition of the interlayer. The Cu–Ni–Ti interlayer significantly changed the morphology of the copper–steel interface, making the transition between the coating and the substrate more continuous and reducing the occurrence of defects. It can be seen from Figure 7b that the Fe-rich phases in the interlayer first grew into plane crystals, and then transformed into columnar dendritic crystals under the influence of supercooling. Plane crystals at the interface formed an Fe-rich band. Figure 7d shows the line-scan results of three interfaces. By comparing the diffusion of elements at the three interfaces, it can be found that the diffusion amount of Fe in coating 2 to the copper layer increased obviously. Therefore, the Cu–Ni–Ti interlayer can promote the diffusion of Fe into the copper matrix coating, which is consistent with the microstructure analysis results.



**Figure 7.** SEM images of bimetallic interface and its element diffusion: (a) interface between steel and copper in coating 1, (b) interface between steel and interlayer in coating 2, (c) interface between interlayer and copper in coating 2, (d) EDS line-scan results of three different interfaces.

### 3.2. Microhardness

The microhardness of coatings 1 and 2 along the cross section is shown in Figure 8. Each hardness value shown in Figure 8 was an average value of three points. The hardness of both coatings is higher than that of the substrate, which indicates that the copper matrix composite coatings designed in this study can effectively improve the surface hardness of Q235 steel. The hardness distribution from the substrate to the coatings shows a trend from low to high in general, but the two curves are different in details. Obviously, this difference is related to the effect of the interlayer. The hardness of coating 1 fluctuates greatly, and the highest hardness is located in the UZ, which is about 414.9 HV<sub>0.1</sub>. In coating 1, the hardness at the bottom of the coating is higher than that at the top, which is related to the diffusion distance of Fe. The farther from the interface, the lower the hardness of the coating due to the less Fe diffused. The hardness of the bottom and top of the coating is basically the same in coating 2 with the interlayer added, because Ni can promote the diffusion of Fe to the top of the coating. In addition, the diffusion of Ni into the coating can also play a role in solid-solution strengthening, which is beneficial to improving the hardness of the coating. There is no abrupt change in hardness at the interface in coating 2, and the hardness transition was relatively smooth. A continuous gradient transition of hardness is realized, and the stress concentration at the interface can be effectively relieved. Therefore, the Cu-Ni-Ti interlayer can significantly improve the hardness distribution characteristics of the copper–steel interface, and achieve a good transition at the bimetallic interface.

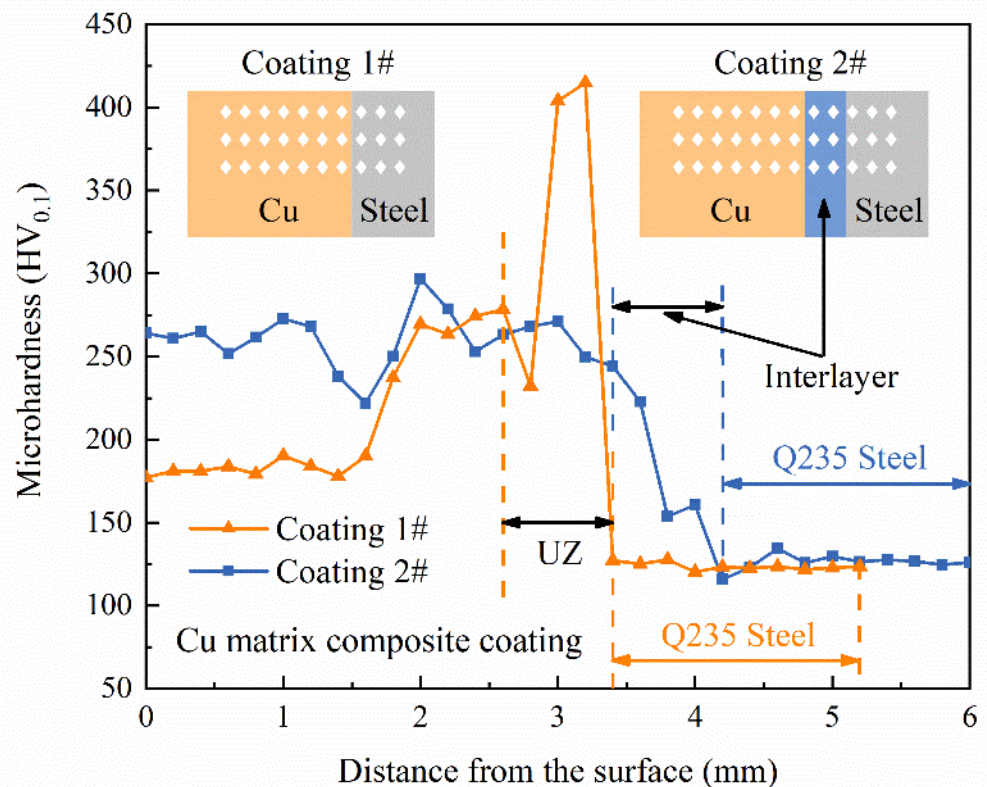


**Figure 8.** Microhardness test results of the coatings.

### 3.3. Wear Behavior

In order to study the effect of the interlayer on the tribological behaviors of copper matrix composite coatings, wear tests were carried out on coatings 1 and 2 and contrast coating. Figure 9 shows the wear test results of three coatings. The average friction coefficients of the copper matrix composite coatings are higher than that of the contrast coating, and the wear losses are much less than contrast coating. The wear loss of coating 1 with the same preparation conditions as the contrast coating (i.e., without the interlayer) is only 42.1% of that of the contrast coating. The results show that the TiC-reinforced copper

matrix composite coatings prepared with flux-cored wires have better wear resistance than commercial aluminum bronze. The wear loss of coating 2 is 4.2% lower than that of coating 1, which indicates that the interlayer is beneficial to improve the wear resistance of the copper matrix composite coatings.

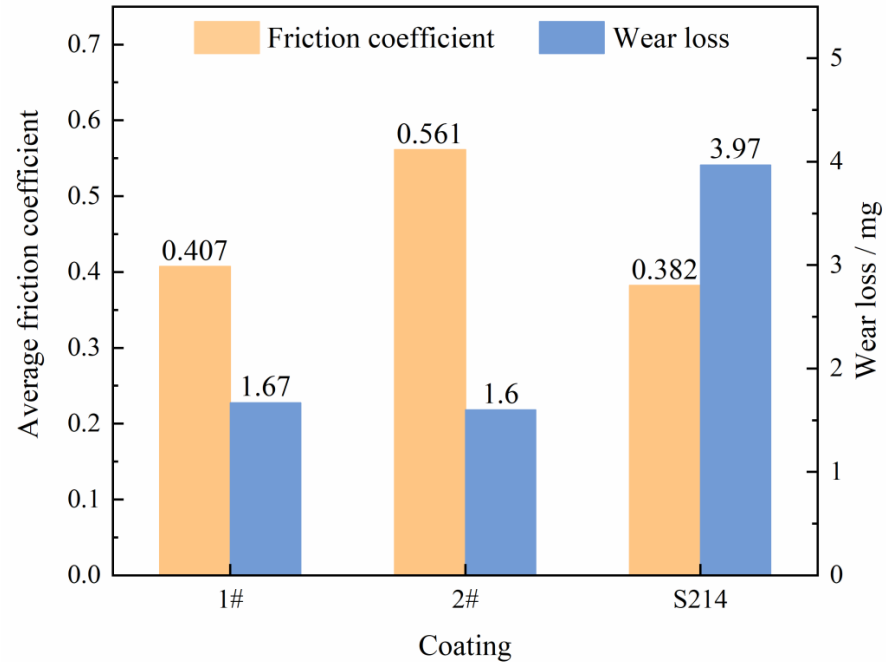


**Figure 9.** Tribological behaviors of the coatings.

Figure 10 shows the wear morphologies of coating 1 and 2. It can be seen that the wear morphologies of the two coatings are different. The EDS analysis results for each spot in Figure 10 are given in Table 4. Figure 10a shows the wear morphology of coating 1, and there are grooves and flakes on the worn surface. EDS analysis result for spot 9 shows that the Ti content on the flake surface is high, which proves that this area may be TiC particles at first. A large number of powdery wear debris was also found on the worn surface. EDS analysis result for spot 10 indicated that the wear debris was mainly oxides. Figure 10b shows the wear morphology of coating 2. Almost no grooves and flakes were found on the worn surface, and the oxide debris (spot 11) was also greatly reduced, which is beneficial to reduce the wear loss. The worn surface of coating 2 is rougher than that of coating 1 due to the presence of more oxide protrusions (spot 12). This may be the main reason for the higher friction coefficient of coating 2.

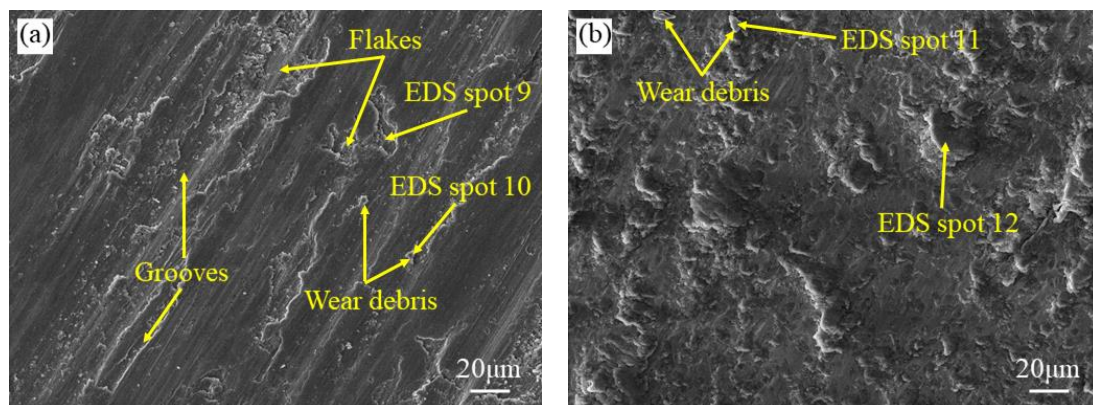


**Figure 10.** Morphologies of the worn samples: (a) coating 1, (b) coating 2.

**Table 4.** EDS analysis results of the worn surfaces (wt.%).

EDS Spots	C K	O K	Al K	Ti K	Fe K	Ni K	Cu K	Sn K
9	0.1	-	1.5	20.4	3.7	-	64.3	10.0
10	-	41.5	-	9.1	7.1	-	40.6	1.7
11	-	55.9	1.5	6.4	8.4	0.8	26.1	1.0
12	0.1	53.8	1.3	6.4	8.6	0.6	27.9	1.2

## 4. Discussion

### 4.1. Effect of the Interlayer on Elimination of High-Hardness UZ

From Figure 8, it can be seen that the hardness in the UZ of coating 1 changes suddenly. EDS analysis was carried out in the region D of the UZ in Figure 7a to explain the phenomenon. An SEM image and element distribution are shown in Figure 11a, and EDS analysis results of each spot in Figure 11a are listed in Table 5. It can be seen that Ti-enriched petal regions exist in the UZ, which is due to the diffusion of Ti in the composite coating into the UZ driven by the concentration gradient (Figure 7d). EDS analysis result of the petal region (spot 13) shows that the region is mainly composed of Fe matrix and Ti-Fe intermetallic compounds (IMCs). Ti-Fe IMCs with high hardness and brittleness will lead to abnormal increase in hardness and brittleness of the UZ. This will worsen the bonding performance of the copper–steel interface and easily lead to stress concentration. The interface will be prone to cracking under the action of stress, which will affect the service life. Therefore, in this paper, abnormal hardness at the interface was reduced and stress concentration was alleviated by eliminating high-hardness UZ.

According to the phase diagrams of Cu-Ni and Fe-Ni [34], Ni has a high solid solubility in both Fe and Cu. Therefore, Ni can promote the mixing of Fe and Cu in the molten pool and increase their mutual solubility [36]. For the above reasons, Cu-Ni-Ti transition material was designed as the interlayer between the copper matrix composite coatings and steel in this study. It can be seen from Figure 7b that after adding the interlayer, the UZ at the copper–steel interface was successfully eliminated due to the adequate mixing of Cu, Fe and Ni. An SEM image of the Cu-Ni-Ti interlayer (region E in Figure 7c) and the element maps are shown in Figure 11b. It was found that Ti is mainly concentrated in inter-dendritic rod-like and equiaxed phases. The EDS test result for spot 14 indicates that these phases may be mixtures of Fe and  $Ti_2Ni$ . After adding the interlayer, the hardness transition between the copper–steel interface became gentler (see Figure 8). The analysis showed that there were three main reasons. Firstly, the Ti-Ni compounds with lower hardness were easier to form than the Fe-Ti compounds with higher hardness due to lower formation enthalpy and Gibbs free energy, so the addition of Ni has an inhibitory effect on the Fe-Ti brittle phases [37]. Secondly, in the Cu-Ni-Fe system, Fe tended to dissolve together with Ni to form dendritic Fe-rich phases, which inhibited the formation of Fe-Ti brittle phases due to the Fe atoms diffused from the substrate were consumed. Finally, the Fe-rich phases and proper amount of the Ti-Ni compounds in the interlayer strengthened the softer copper matrix, which increased the hardness of the interlayer between the composite coating and the steel substrate. Thus, gradient transition was realized by adding the interlayer, and the adverse effects of the abrupt change of interface hardness on mechanical properties was avoided.

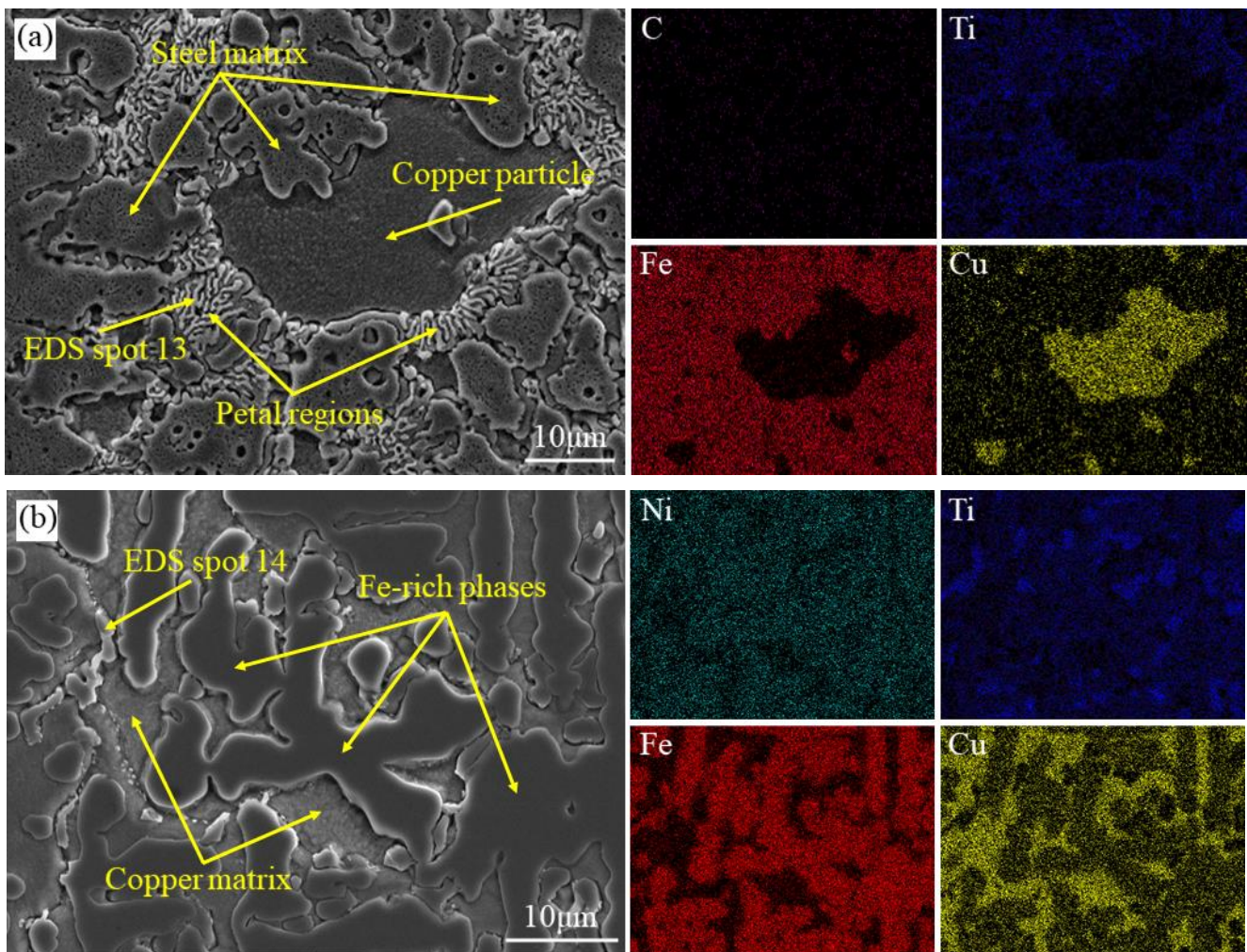


**Figure 11.** SEM images and elemental maps of the UZ and interlayer: (a) region D in Figure 7a of the UZ, (b) region E in Figure 7c of the interlayer.

**Table 5.** EDS analysis results of the UZ and the interlayer (wt.%).

EDS Spots	C K	Al K	Ti K	Fe K	Ni K	Cu K	Sn K
13	-	3.3	8.5	83.1	-	4.9	0.1
14	-	1.7	28.1	49.5	13.3	6.1	1.3

#### 4.2. Effect of the Interlayer on Inhibiting LME Cracks

Figure 12a shows the formation mechanism of LME cracks at the copper–steel interface. During the arc cladding process, when the temperature is higher than the melting point of copper but lower than that of iron, liquid copper tends to wet the austenite grain boundaries of steel because of the small dihedral angle (about  $18^\circ$ ) between liquid copper and solid iron [38]. Driven by the difference in electronegativity, charges transfer from Fe atoms to Cu atoms, thereby weakening the Fe–Fe bonds within the austenite grain boundaries. This leads to the reduction of critical stress required for grain boundary cracking, which makes it easier to crack [39]. Then, the LME cracks are formed at the grain boundaries of steel when the thermal stress exceeded the critical stress. After adding the interlayer, no LME cracks were found at the interface, as shown in Figure 4a. The result shows that Ni can inhibit the formation of LME cracks, which is consistent with the results of [24,40]. The inhibition of Ni on LME cracks at the copper–steel interface is related to the interface structure, as shown in Figure 12b. Near the interface, the Fe-rich phases in the interlayer first solidified

in a planar crystal manner. As a result, an Fe-rich band was formed, which is essentially a solid solution formed by Fe, Ni, Cu, and a few other elements. From the element maps in Figure 11b, it can be seen that Cu in the interlayer mainly exists in the intergranular of the Fe-rich phases, and the content in the Fe-rich phases is less. Therefore, the Fe-rich band at the interface acted as a barrier between the steel substrate and the copper-rich liquid. This reduces the possibility of LME cracking because the number of liquid Cu atoms contacting with the solid-steel matrix was greatly reduced. In the following study, we will characterize the microstructure of the Fe-rich band in more detail and further explore the mechanism of Fe-rich bands inhibiting LME cracks.

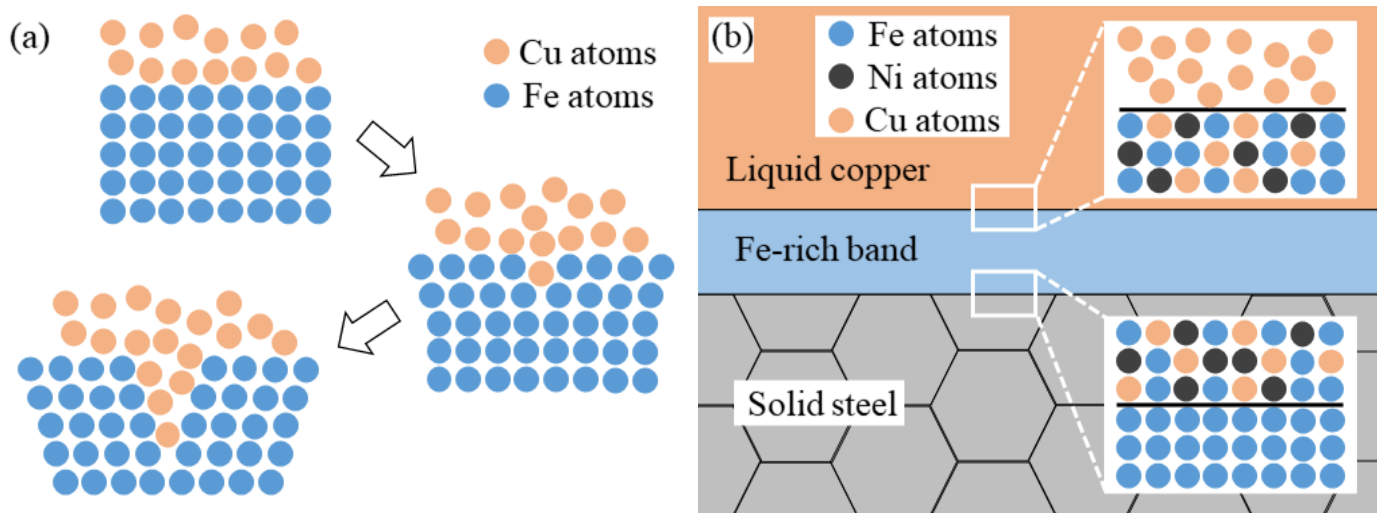


**Figure 12.** Schematic diagram of (a) LME crack-formation mechanism and (b) inhibition of LME cracks by Fe-rich band.

#### 4.3. Effect of Interlayer on Properties of Composite Coatings

In this study, the hardness of coating 2 was higher than that of coating 1, which indicates that the interlayer had a significant strengthening effect on the composite coatings. The strengthening mechanism is mainly embodied in the following three aspects. Firstly, the Ni element in the interlayer dissolved into the copper matrix, which produced a certain solid solution-strengthening effect. Secondly, the number of Fe-rich phases in the coating increased due to the interlayer that promoted the diffusion of iron into copper. This enhanced the second phase-strengthening effect of the Fe-rich phases relative coating. Thirdly, fine grain strengthening occurred due to the increase of the Fe-rich phases in the coating that hindered the growth of copper grains. In summary, the improvement of coating hardness is the result of the combined action of solid solution strengthening, second-phase strengthening, and fine grain strengthening. The increase in hardness is beneficial to improve the wear resistance of the coatings [41]. It can be seen from Figure 10a that the worn surface of coating 1 is seriously flaking. This is because when the surface of the coating was in contact with the friction pair, the material fell off the matrix due to the welding-tearing process under large local stress and relative movement. Wear debris would be oxidized quickly when it came into contact with air at high temperatures. Wear was exacerbated by oxides and exfoliated TiC particles ploughing grooves on the friction surface. The wear mechanism of coating 1 mainly included adhesive wear, abrasive wear, and oxidative wear. With the addition of the Cu-Ni-Ti interlayer, the copper matrix was strengthened because of the dissolution of Ni. On the one hand, the wear of the copper matrix can be reduced. On the other hand, it can strengthen the coating effect of the matrix on the hard phases, which is beneficial to reduce the shedding of the hard particles. The above analysis is confirmed because almost no grooves and flakes were found in coating 2 from Figure 10b. In addition, the increase in Fe-rich phases is beneficial to reduce the wear loss of the coating, because it can play a better supporting role during the wear process.

## 5. Conclusions

In this paper, TiC-reinforced copper matrix composite coatings with and without a Cu-Ni-Ti interlayer were prepared on Q235 low-carbon steel by GTA cladding. The effects of the interlayer on the microstructure, interfacial bonding behavior, hardness and wear resistance of the composite coatings were studied. The results are summarized as follows.

(1) The composite coatings were mainly composed of  $\alpha$ -Cu, TiC and Fe-rich phases. After the interlayer was added, some Ni elements were dissolved in the copper matrix, which promoted the diffusion of Fe into the coating. This increased the number of Fe-rich phases in the coating and refined the  $\alpha$ -Cu grains.

(2) When the copper matrix composite coatings were deposited directly on the steel, high-hardness UZ was formed at the interface due to the insufficient mixing of copper and iron and the diffusion of Ti. After the interlayer was added, UZ was eliminated due to the promotion of molten pool mixing. Ti-Ni IMCs with lower hardness was formed in the interlayer, which inhibited the formation of Ti-Fe IMCs with high hardness and realized the gradient transition.

(3) Due to the weakening of the steel grain boundaries by the liquid copper and the effect of thermal stress, many LME cracks appeared at the interface without the interlayer. After adding the interlayer, the Fe-rich solid solution band was formed at the interface. Thus, the LME cracks were inhibited due to the reduced contact of the liquid copper with the steel matrix.

(4) With the addition of the interlayer, the hardness of the composite coating was improved by the combination of solid solution strengthening, second phase strengthening and fine grain strengthening. The wear loss of the coating was reduced. Therefore, adding an interlayer can improve the wear resistance of TiC-reinforced copper matrix composite coatings.

**Author Contributions:** Methodology, J.L. and M.Z.; validation, J.L. and Z.Z.; data curation, L.L. and Z.Z.; writing—original draft preparation, L.L.; writing—review and editing, L.L. and M.D.; project administration, M.Z. All authors have read and agreed to the published version of the manuscript.

**Funding:** This research was funded by the National Natural Science Foundation of China (grant 51974243) and Xi'an Municipal Science and Technology Planning Project (grant 21XJZZ0057).

**Institutional Review Board Statement:** Not applicable.

**Informed Consent Statement:** Not applicable.

**Data Availability Statement:** Data are contained within the article.

**Conflicts of Interest:** The authors declare no conflict of interest.

## References

1. Jie, J.C.; Liu, C.B.; Wang, S.H.; Dong, B.W.; Liu, S.C.; Li, T.J. Characterisation of steel/nickel bronze clad strips prepared by continuous solid/liquid bonding method. *Mater. Sci. Technol.* **2019**, *35*, 1840–1847. [[CrossRef](#)]
2. Zhang, M.; Zhang, Y.L.; Li, J.; Zhang, S.F.; Du, M.K.; Wang, G. Microstructure and mechanical properties of the joint fabricated between stainless steel and copper using gas metal arc welding. *Trans. Indian Inst. Met.* **2021**, *74*, 969–978. [[CrossRef](#)]
3. Chen, S.H.; Yu, X.H.; Huang, J.H.; Yang, J.; Lin, S.B. Interfacial ferrite band formation to suppress intergranular liquid copper penetration of solid steel. *J. Alloys Compd.* **2019**, *773*, 719–729. [[CrossRef](#)]
4. Chang, C.C.; Wu, L.H.; Shueh, C.; Chan, C.K.; Shen, I.C.; Kuan, C.K. Evaluation of microstructure and mechanical properties of dissimilar welding of copper alloy and stainless steel. *Int. J. Adv. Manuf. Technol.* **2017**, *91*, 2217–2224. [[CrossRef](#)]
5. Najafi, S.; Khanzadeh, M.R.; Bakhtiari, H.; Seyedraoufi, Z.S.; Shajari, Y. Electrochemical investigation of dissimilar joint of pure Cu to AISI 410 martensitic stainless steel fabricated by explosive welding. *Surf. Eng. Appl. Electrochem.* **2020**, *56*, 675–683. [[CrossRef](#)]
6. Sabetghadam, H.; Hanzaki, A.Z.; Araee, A.; Hadian, A. Microstructural evaluation of 410 SS/Cu diffusion-bonded joint. *J. Mater. Sci. Technol.* **2010**, *26*, 163–169. [[CrossRef](#)]
7. Bai, Y.C.; Zhang, J.Y.; Zhao, C.L.; Li, C.J.; Wang, H. Dual interfacial characterization and property in multi-material selective laser melting of 316L stainless steel and C52400 copper alloy. *Mater. Charact.* **2020**, *167*, 110489. [[CrossRef](#)]
8. Cheng, Z.; Liu, H.; Huang, J.H.; Ye, Z.; Yang, J.; Chen, S.H. MIG-TIG double-sided arc welding of copper-stainless steel using different filler metals. *J. Manuf. Process.* **2020**, *55*, 208–219. [[CrossRef](#)]

9. Li, Y.N.; Liu, X.B.; Zhou, Z.K.; Zhang, L.; Peng, Z.L.; Robert, B.H. The microstructure and wear resistance of a copper matrix composite layer on copper via nitrogen-shielded arc cladding. *Coatings* **2016**, *6*, 67. [[CrossRef](#)]
10. Besnea, D.; Dontu, O.; Avram, M.; Spănu, A.; Rizescu, C.; Pascu, T. Study on laser welding of stainless steel/copper dissimilar materials. *IOP Conf. Ser. Mater. Sci. Eng.* **2016**, *147*, 012047. [[CrossRef](#)]
11. Ramachandran, S.; Lakshminarayanan, A.K. An insight into microstructural heterogeneities formation between weld subregions of laser welded copper to stainless steel joints. *Trans. Nonferrous Met. Soc. China* **2020**, *30*, 727–745. [[CrossRef](#)]
12. Xu, H.; Xu, M.J.; Yu, C.; Lu, H.; Wei, X.; Chen, J.M.; Xu, J.J. Effect of the microstructure in unmixed zone on corrosion behavior of 439 tube/308L tube-sheet welding joint. *J. Mater. Process. Technol.* **2017**, *240*, 162–167. [[CrossRef](#)]
13. Devendranath, R.K.; Patel, S.D.; Sri, P.S.; Choudhury, D.J.; Prabakaran, P.; Arivazhagan, N.; Xavier, M.A. Influence of filler metals and welding techniques on the structure–property relationships of Inconel 718 and AISI 316L dissimilar weldments. *Mater. Des.* **2014**, *62*, 175–188. [[CrossRef](#)]
14. Zhang, Q.Y.; Dong, Q.P.; Wang, X.N.; Wang, Z.J.; Sun, D.K.; Zhu, M.F.; Qian, Y.H.; Hiromi, N. Predictions of solute mixing in a weld pool and macrosegregation formation during dissimilar-filler welding of aluminum alloys: Modeling and experiments. *J. Mater. Res. Technol.* **2020**, *9*, 12080–12090. [[CrossRef](#)]
15. Gan, Z.T.; Yu, G.; He, X.L.; Li, S.X. Numerical simulation of thermal behavior and multicomponent mass transfer in direct laser deposition of Co-base alloy on steel. *Int. J. Heat Mass Transfer* **2017**, *104*, 28–38. [[CrossRef](#)]
16. Adomako, N.K.; Kim, J.H. Microstructure and mechanical properties of dissimilar laser lap joint between CoCrFeMnNi-high entropy alloy and duplex stainless steel. *Mater. Lett.* **2021**, *288*, 129354. [[CrossRef](#)]
17. Cheng, Z.; Huang, J.H.; Ye, Z.; Chen, Y.; Yang, J.; Chen, S.H. Microstructures and mechanical properties of copper-stainless steel butt-welded joints by MIG-TIG double-sided arc welding. *J. Mater. Process. Technol.* **2019**, *265*, 87–98. [[CrossRef](#)]
18. Meng, Y.F.; Li, X.W.; Gao, M.; Zeng, X.Y. Microstructures and mechanical properties of laser-arc hybrid welded dissimilar pure copper to stainless steel. *Opt. Laser Technol.* **2019**, *111*, 140–145. [[CrossRef](#)]
19. Switzner, N.; Queiroz, H.; Duerst, J.; Yu, Z. Si-bronze to 304 stainless steel GTA weld fusion zone microstructure and mechanical properties. *Mater. Sci. Eng. A* **2018**, *709*, 55–64. [[CrossRef](#)]
20. Soysal, T.; Kou, S.; Tat, D.; Pasang, T. Macrosegregation in dissimilar-metal fusion welding. *Acta Mater.* **2016**, *110*, 149–160. [[CrossRef](#)]
21. Zhang, M.; Zhang, Y.L.; Du, M.K.; Zhang, S.F.; Lei, L.Y. Experimental characterization and microstructural evaluation of silicon bronze-alloy steel bimetallic structures by additive manufacturing. *Metall. Mater. Trans. A* **2021**, *52*, 4664–4674. [[CrossRef](#)]
22. Rahman, A.; Abdel, R.N.A.; El, K.M.R. Effect of heat input on the microstructure and properties of dissimilar weld joint between Incoloy 28 and superaustenitic stainless steel. *Acta Metall. Sin.* **2014**, *27*, 259–266. [[CrossRef](#)]
23. Khan, W.N.; Chhibber, R. Effect of filler metal on solidification, microstructure and mechanical properties of dissimilar super duplex/pipeline steel GTA weld. *Mater. Sci. Eng. A* **2021**, *803*, 140476. [[CrossRef](#)]
24. Chun, E.J.; Lee, J.H.; Kang, N. Unmixing behaviour in dissimilar laser welds for duplex and austenitic stainless steels. *Sci. Technol. Weld. Joining* **2019**, *24*, 263–275. [[CrossRef](#)]
25. Sun, Z.C.; Li, P.Y.; Zhang, T.; Wang, J.B.; Xu, D.; Chen, H.; Liu, D.H.; Pei, Y.Y. Effect of stress and Si on liquid metal embrittlement of 316L (N)-copper. *Mater. Sci. Technol.* **2021**, *37*, 552–559. [[CrossRef](#)]
26. Wang, J.; de Castro, C.C.; Lu, X.F. The formation mechanisms and improvement measures for penetrating cracks in QA19-4/Q345B welded joint. *J. Mater. Eng. Perform.* **2020**, *29*, 2346–2354. [[CrossRef](#)]
27. Magnabosco, I.; Ferro, P.; Bonollo, F.; Arnberg, L. An investigation of fusion zone microstructures in electron beam welding of copper–stainless steel. *Mater. Sci. Eng. A* **2006**, *424*, 163–173. [[CrossRef](#)]
28. Cao, S.L.; Liang, J.; Wang, L.Q.; Zhou, J.S. Effects of NiCr intermediate layer on microstructure and tribological property of laser cladding Cr<sub>3</sub>C<sub>2</sub> reinforced Ni60A-Ag composite coating on copper alloy. *Opt. Laser Technol.* **2021**, *142*, 106963. [[CrossRef](#)]
29. Liu, F.; Liu, C.S.; Chen, S.Y.; Tao, X.Q.; Zhang, Y. Laser cladding Ni–Co duplex coating on copper substrate. *Opt. Lasers Eng.* **2010**, *48*, 792–799. [[CrossRef](#)]
30. Shi, Z.P.; Wang, Z.B.; Wang, J.Q.; Qiao, Y.X.; Chen, H.N.; Xiong, T.Y.; Zheng, Y.G. Effect of Ni interlayer on cavitation erosion resistance of NiTi cladding by tungsten inert gas (TIG) surfacing process. *Acta Metall. Sin.* **2020**, *33*, 415–424. [[CrossRef](#)]
31. Zhang, X.C.; Sun, C.; Pan, T.; Flood, A.; Zhang, Y.L.; Li, L.; Liou, F. Additive manufacturing of copper–H13 tool steel bi-metallic structures via Ni-based multi-interlayer. *Addit. Manuf.* **2020**, *36*, 101474. [[CrossRef](#)]
32. Li, J.H.; Zhang, Y.L.; Du, M.K.; Zhang, M.; Li, J.; Lei, L.Y. Effect of alloy elements on the interface connection mechanism and properties of copper/steel welded joints. *Trans. China Weld. Inst.* **2021**, *42*, 34–41+100.
33. Alfredo, M.; Oscar, P.; Jhon, O. Influence of gas pressure on the mechanical and tribological properties of Cu–Al coatings deposited via thermal spray. *Coatings* **2019**, *9*, 722.
34. Manu, K.; Jezierski, J.; Ganesh, M.R.S.; Shankar, K.V.; Narayanan, S.A. Titanium in cast Cu–Sn alloys—A review. *Materials* **2021**, *14*, 4587. [[CrossRef](#)] [[PubMed](#)]
35. Zhang, D.D.; He, X.Y.; Liu, Y.; Bai, F.; Wang, J.G. The effect of in situ nano-sized particle content on the properties of TiCx/Cu composites. *J. Mater. Res. Technol.* **2021**, *10*, 453–459. [[CrossRef](#)]
36. Gan, W.P.; Jin, Z.P. Miscibility gap in the Fe–Cu–Ni system at 1173 K. *J. Mater. Sci. Technol.* **1992**, *3*, 181–184.
37. Mou, G. *Study on Microstructure Control of Interface Layer and Properties of TC4/304L Joints Fabricated by CMT*; Shanghai Jiao Tong University: Shanghai, China, 2020.

38. Van, V.L.H. Intergranular energy of iron and some iron alloys. *J. Met.* **1951**, *3*, 251–259.
39. Yuasa, M.; Mabuchi, M. Effects of segregated Cu on an Fe grain boundary by first-principles tensile tests. *J. Phys. Condens. Matter.* **2010**, *22*, 505705. [[CrossRef](#)] [[PubMed](#)]
40. Chen, C.; Zhou, J.; Xue, F.; Wu, Q.P. Elimination of liquid metal embrittlement cracks during arc cladding of tin bronze on steel sheet. *Mater. Lett.* **2020**, *269*, 127646. [[CrossRef](#)]
41. Yang, L.; Yu, T.B.; Li, M.; Zhao, Y.; Sun, J.Y. Microstructure and wear resistance of in-situ synthesized Ti (C, N) ceramic reinforced Fe-based coating by laser cladding. *Ceram. Int.* **2018**, *44*, 22538–22548. [[CrossRef](#)]